Depth-Aware Motion Deblurring Using Loopy Belief Propagation

Bin Sheng, Ping Li, Xiaoxin Fang, Ping Tan, and Enhua Wu, *Member, IEEE*

***Abstract*—Most motion-blurred images captured in the real world have spatially-varying point-spread functions, and some are caused by different positions and depth values, which cannot be handled by most state-of-the-art deblurring methods based on deconvolution. To overcome this problem, we propose a depth-aware motion blur model that treats a blurred image as an integration of a sequence of clear images. To restore the clear latent image, we extend the Richardson-Lucy method to incorporate our blur model with a given depth image. The empty holes in the depth image, caused by occlusion or device limitations, are fixed by PatchMatch-based depth filling. We regard the depth image as a Markov random field and select candidate labels by using belief propagation to set and smooth depth values for empty areas. Deblurring and depth filling are performed iteratively to refine the results. Our method can also be applied to real-world images with the assistance of motion estimation. The deblurring process is shown to be convergent; moreover, the number of iterations and the level of noise amplification are acceptable. The experimental results show that our method can not only handle depth-variant motion blur but also refine depth images.**

***Index Terms*—Deblur, depth-variant, Richardson-Lucy.**

I. Introduction

MOTION blur is a common problem in images captured by hand-held cameras. Blurring occurs when relative motion exists between the camera and the objects being recorded during exposure. Information in images may be lost due to motion blur. Thus, restoring clear latent image from a blurred input is critical. A simple assumption about motion blur is to regard a blurred image as the convolution result of a clear image and a point-spread function (PSF). The deconvolution problem can be solved by optimization or inverse Fourier transformation. However, the assumption of convolution with PSF simplifies motion blur into a spatially invariant problem, which is nearly impossible in real cases for two reasons. One is that motions such as zoom-in (zoom-out) or rotation will lead to different pixels having different motion paths. The other is that PSF varies with the depth values of objects, objects close to the camera suffer from more severe blurring than those far away. Some methods [1]–[4] attempt to segment an image into several regions and set a constant PSF for each region. However, these segments should be small enough to ensure that all regions have similar PSFs, which is neither suitable for complicated scenes nor conducive to pixel-wise deblurring. Although optimization methods can solve such problems by setting a different PSF for each pixel, the large number of pixels leads to time-consuming computation.

We propose a depth-aware motion blur model based on [5]. Our blur model treats a blurred image as an integration of a sequence of clear images. Each frame of the sequence is obtained by applying a transformation to the initial clear frame, which is from the transformation in 3D space. From the viewpoint of each pixel, it is implemented by multiplying the pixel's coordinate with a transformation matrix. One assumption in our method is that the depth map obtained is at least less blurred compared to the color image, which could provide additional useful information in deblurring. With the assistance of the depth, the motion of each pixel is considered in three dimensions to simulate spatially variant PSFs, and the deblurring quality could be enhanced (see Fig. 1). As the transformation is applied to each pixel, spatially-varying PSFs

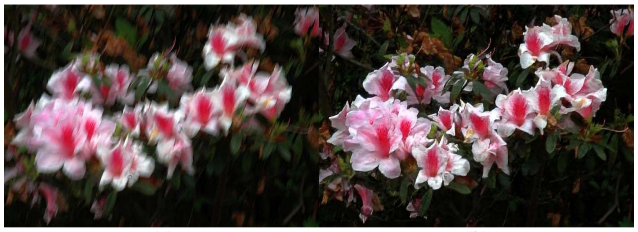

Fig. 1. Depth-aware motion deblurring. (a) Input blur image with spatially-varying motion blur. (b) Our depth-aware motion deblurring result.

Manuscript received June 10, 2017; revised December 24, 2017, September 25, 2018 and January 17, 2019; accepted February 22, 2019. Date of publication February 26, 2019; date of current version April 3, 2020. This work was supported in part by the National Natural Science Foundation of China under Grant 61872241 and Grant 61572316, in part by the National Key Research and Development Program of China under Grant 2017YFE0104000 and Grant 2016YFC1300302, in part by the Macau Science and Technology Development Fund under Grant 0027/2018/A1, and in part by the Science and Technology Commission of Shanghai Municipality under Grant 18410750700, Grant 17411952600, and Grant 16DZ0501100. This paper was recommended by Associate Editor Y. Wu. *(Bin Sheng and Ping Li contributed equally to this work.) (Corresponding author: Bin Sheng.)*

B. Sheng is with the Department of Computer Science and Engineering, Shanghai Jiao Tong University, Shanghai 200240, China, and also with the MoE Key Lab of Artificial Intelligence, AI Institute, Shanghai Jiao Tong University, Shanghai 200240, China (e-mail: shengbin@sjtu.edu.cn).

P. Li is with the Faculty of Information Technology, Macau University of Science and Technology, Macau 999078, China (e-mail: pli@must.edu.mo).

X. Fang is with the Department of Computer Science and Engineering, Shanghai Jiao Tong University, Shanghai 200240, China.

P. Tan is with the School of Computing Science, Simon Fraser University, Burnaby, BC V5A 1S6, Canada (e-mail: pingtan@sfu.ca).

E. Wu is with the State Key Laboratory of Computer Science, Institute of Software, Chinese Academy of Sciences, Beijing 100190, China, and also with the University of Macau, Macau 999078, China (e-mail: ehwu@um.edu.mo).

Color versions of one or more of the figures in this article are available online at http://ieeexplore.ieee.org.

Digital Object Identifier 10.1109/TCSVT.2019.2901629

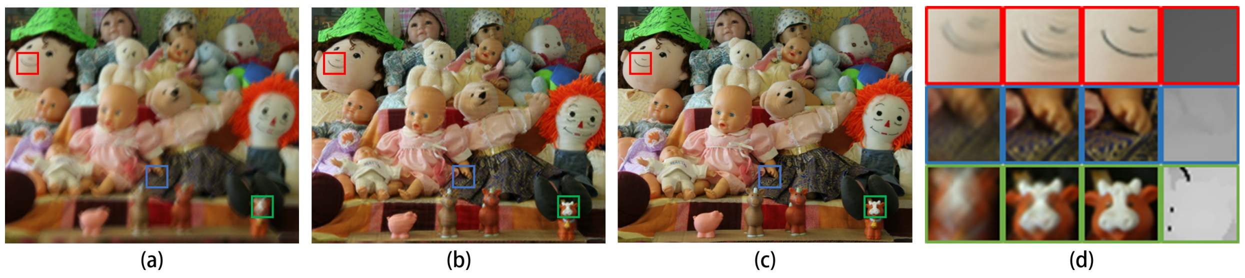

Fig. 2. Our deblurring result. (a) Input blur image with spatially-varying motion blur for objects with different depths. (b) Our result with depth refinement after every 10 iterations of intermediate image updating. (c) Ground-truth image. (d) Close-up view of the three images, with related depths on the right.

are perfectly obtained. We extend the Richardson-Lucy (RL) method [6] and make it applicable to spatially variant motion blur in 3D space. One problem in considering the depth is that most depth images captured by current devices contain empty holes. In our deblurring model, each frame of the latent clear image sequence should have its corresponding depth map, which is obtained by applying the same transformation to the initial clear depth map. We use a PatchMatch-based method to fill these holes. Then, belief propagation is used to smooth the edges and reduce the noise in the intermediate results.

We separate the entire framework into two subproblems. In the depth filling, the latent clear image is set to be constant and is obtained from the intermediate results of certain deblurring iterations. In the deblurring, the depth image is given by the filling result. Deblurring and depth filling are performed iteratively to refine the clear images as well as the depth map. Fig. 2 shows the deblurring results of our approach for spatially variant blur with varying depth for the "dolls" scene. Our work makes the following three main contributions:

- We propose a motion blur model that takes depth into consideration and synthesizes blurred images with spatially variant blur caused by three-dimensional motion.
- We propose a new method to fill the empty holes in a depth image during blur synthesis, which can predict sharp and accurate edges in the depth image.
- We present a deblurring method for our blur model. Our deblurring can restore images suffering from pixel-level spatially variant blur. Moreover, it is robust against noise.

II. Related Work

Depending on whether the PSF is given, image deblurring is categorized into two main types: blind deblurring (without PSF) and non-blind deblurring (with PSF). As the PSFs can be uniform or non-uniform, deblurring can be further categorized into spatially invariant or spatially variant problems. Most previous studies have focused on blur models with spatially invariant PSFs. Non-blind deblurring methods can restore latent images given the blurred images and the corresponding PSFs. In such cases, the blurred images can be synthesized with the ground-truth blur kernel. Traditional methods, such as the Wiener filter [7] and Richardson-Lucy algorithm [6] have attempted to minimize the difference between the convolution results of latent and blurred images. These methods suffer from ringing artefacts due to the loss of high-frequency details. The noise will also be amplified in the optimization and deconvolution. To overcome these problems, regulation terms are used to constrain the restored image. Chan and Wong [8] proposed the use of the L1 norm of the image gradient as the regularization term. Levin *et al.* [9] extended this method such that the regularization term can be any power of the image gradient as the Hyper-Laplacian term. In [10], threads were set and different terms were applied for different gradient values.

Compared to blind deblurring, non-blind deblurring involves the estimation of the blur kernel directly. Reference [8] employed the Laplacian regularization term for estimating the PSF. In [11], pit has been shown that the forementioned method may yield a deblurring result that is the same as the source blurred image, and the PSF is a single point with a central value of 1. Thus, in [12], an approach for estimating the PSF according to the transparency of the blurred object edges was proposed. Recent methods, such as [10] and [13], combined deblurring and kernel estimation, and performed the two processes iteratively to obtain the final latent image. Fourier transformation [14] or Iteratively Re-weighted Least Squares (IRLS) [15] can be used to solve these optimization problems. However, these methods cannot handle images with spatially-variant PSFs.

The forementioned methods use blurred image as the only image reference, and the deblurring quality varies. To obtain additional details about the latent image, a highly noisy clear image captured with a short exposure time was used to guide the deblurring [16]. In [4], two images with different resolutions were captured, and a low-resolution high-frequency image was used to guide the restoration of the high-resolution blurred images. In [17], three different camera models were used to improve the image quality. However, these methods require complicated devices. In [18], a method for sharp image estimation based on the depth-involved motion-blurred images is proposed. However, their method works on estimating the PSF for each pixel, they hence calculate a PSF shape for the whole image. Our approach focuses on restoring clear latent images by extending the Richardson-Lucy method to incorporate our blur model with a given depth image. Since depth maps may contain hole-regions caused by occlusion or device limitations, we propose hole-filling techniques via PatchMatch and loopy belief propagation with joint-bilateral filtering (JBF) for depth refinement to obtain smooth depth values for our depth-aware motion deblurring.

Recently, a method for estimating a spatially variant kernel was proposed [19]. In [1], image segmentation was used to set different PSFs for different layers. Tai *et al.* [20] used a hybrid camera framework and estimated one PSF per pixel, but this approach requires an auxiliary video camera. Machine learning was used in [21] and [22] to perform deblurring. However, the learning methods require the training and testing sets to have similar blur kernels; otherwise, the deblurring result is invalid. We propose a depth-aware motion blur model based on [5] in order to obtain pixel-level spatially variant PSFs. The depth values play an important role in improving the deblurring results, which makes it possible to simulate the motion path in three dimensions in the real world. Unlike [23], which uses depth to segment the image into layers, our method directly applies the depth value of each pixel to deblur that pixel. We also propose a new inpainting method for depth images based on PatchMatch and Markov random field (MRF) belief propagation to solve the problem of empty holes in real captured depth images. Although our method is a non-blind deblurring based on the RL algorithm [6], it can be extended to real cases with kernel estimation under user assistance.

III. Approach Overview

Motion blur in real captured images is due to the relative motion between the objects being captured and the camera during the exposure time. The information for each pixel is the integration of the light incident on it during this period. The final image can be expressed as the integration of the light intensity with respect to time:

$$I = \int_0^T I(t)dt \tag{1}$$

where, I is the final image and $I(t)$ is the light information at time t. Note that $I(t)$ may be infinite in real cases, which is not suitable for image processing. Hence, we represent it in discrete form as the sum of n image frames:

$$I = \frac{1}{n}\sum_{i=1}^{n} I(i) \tag{2}$$

where, all the light information in Eq. (1) is split into n parts. Each image frame is light integration result in a short period:

$$I(i) = \int_{(i-1)T/n}^{iT/n} I(t)dt \tag{3}$$

When the objects captured by the camera are static during exposure period, blurring occurs only because of the motion of the camera itself. With this assumption, the image information $I(i)$ for each i can be regarded as the transformation result of the initial image information $I(0)$. To be more general, $I(0)$ is a three-dimensional image with depth information. Then, we can perform transformation from the 3D space to its projective space assuming perspective projection using a transformation matrix P [24], and further apply a homography H_i for the transformation of the projective space. Thus, we have our transformation matrix $M_i = H_i P$, where $H_i = \prod_{j=1}^{i} h_j$. Here, h_j is a homography defined by a 3×3 nonsingular matrix up to a scalar, and we use a homography for its ability to model all planar transformations [5]. Therefore, M_i is the transformation using the 3D space and slice motion. Based on transformation matrix M_i, each pixel in $I(i)$ can get its corresponding position in initial image $I(0)$:

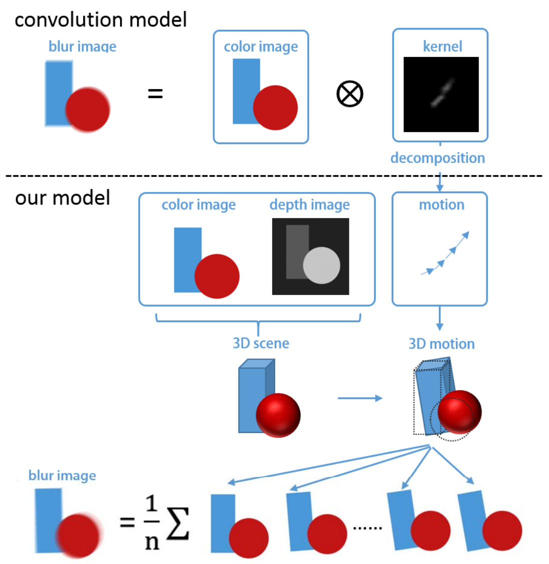

Fig. 3. Comparison between traditional convolutional model and our matrix-based motion blur model. The traditional model generates blurred image using convolution result of clear image and the blur kernel. Our model sums up several intermediate frames of clear images by transformation matrices using 3D space and slice motion. Thus, the blurriness of each pixel in our model is affected by the transformation matrices, pixel positions, and depth values.

$$I(p, i) = I(M_i p, 0) \tag{4}$$

In this equation, p is the coordinate of pixels in $I(i)$ and M_i is the matrix that transforms $I(0)$ into $I(i)$ from the 3D space to the projective space. Through this representation, the blur image I_b can be obtained using only initial clear image $I(0)$ and n transformation matrix M_1 to M_n as follows:

$$I_b(p) = \frac{1}{n}\sum_{i=1}^{n} I(M_i p, 0) \tag{5}$$

Fig. 3 compares our matrix-based blur model with the convolutional model. Our model generates the transformation matrices from the blur kernel. In this case, the deblurring problem becomes the problem of estimating the clear result $I(0)$ given the blurred image I_b and all matrices M. We will now show the advantage of our matrix-based blur model over the kernel-based model. The commonly used convolution form for image blur synthesis can be expressed as:

$$I_b = I \otimes K \tag{6}$$

where, K is the blur kernel, which is also called the point-spread function (PSF). This model assumes that all pixels pass through the same path during the exposure time, which is nearly impossible because of camera jitter. For example, it cannot synthesize camera rotation, in which case the center pixel remains static and the pixels in the four corners of the image move considerably. However, by using the matrix form

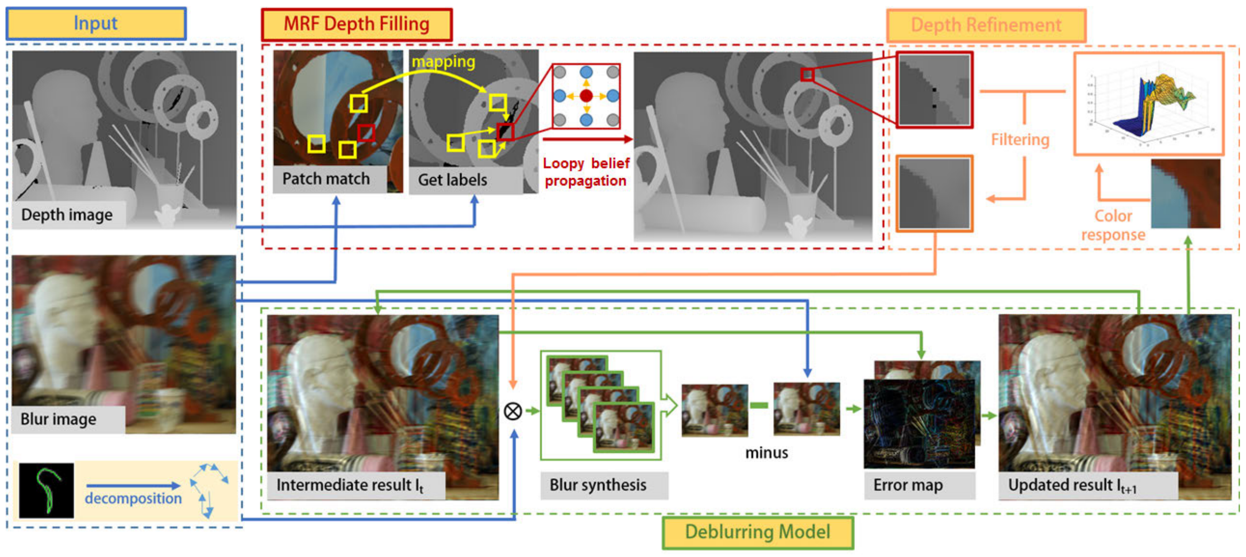

Fig. 4. Approach framework for our deblurring method. Our approach takes the initial depth image and motion-blurred image as inputs. In each iteration, we use the current estimated latent image I^t as the clear image to fill the empty areas in the initial depth image. Then, we compute a synthetic blurred image according to I^t, filled depth image, and transformation matrices. The error image is then estimated using the synthesized blurred image and the initial motion-blurred image. Using the estimated error, the latent image is updated to image I^{t+1}. Then I^{t+1} is used to process the next iteration.

shown in Eq. (5), we can achieve translation, rotation, and scaling at the same time by using different matrices M.

Using matrix-based motion blur model, we propose our corresponding deblurring framework, as shown in Fig. 4. The input part includes depth image, blurred image, and blur kernel. Our model decomposes the blur kernel into several transformation matrices to synthesize the blurred image, as shown in kernel decomposition. To solve the problem of information loss in depth images, we use the depth image and blurred image as inputs to predict depth values of the empty holes in the initial depth map, as described in Section IV (See the MRF depth filling part in Fig. 4). In the depth refinement part, we use the intermediate deblurring result to refine the depth map, as described in Section IV-C. The deblurring part shows how we update the deblurring result iteratively. First, we synthesize the blurred image using the transformation matrix obtained from the input, as described in Section V-B. Then, we perform deblurring with the assistance of the depth image. The details of the deblurring model are given in Section V.

IV. MRF Depth Filling

In general, we cannot obtain perfect depth image that provides depth values for each pixel. Some empty holes usually exist because of occlusion or limitations of depth cameras. Our method assumes the depth filling problem as an optimization problem that aims to minimize the following energy:

$$E_{total} = \sum_{p} E(p, D(p)) \qquad (7)$$

where, $E(p, D(p))$ is the energy for pixel p with depth value $D(p)$. For an 8-bit depth image, depth value $D(p)$ can have 255 choices. There are numerous pixels in an image, whose energies can affect one another. It is impossible to obtain an accurate solution for Eq. (7). Instead, to obtain the global minimum, we assume that each pixel is related only to its neighbor pixels and regard the image as a Markov random field (MRF). A MRF is an undirected graphical model that can encode spatial dependencies. Each pixel is represented as one node in this undirected graph and is connected to its four immediate neighbors, namely, up, down, right, and left (See Fig. 5). Under this assumption, the optimization problem for minimizing Eq. (7) can be solved by loopy belief propagation (LBP), which will be described later.

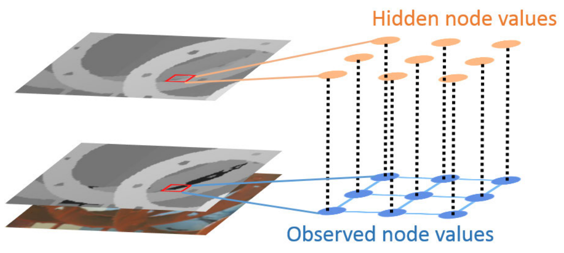

Fig. 5. Markov Random Field for a 3×3 image. The observable node variables in our case correspond to the initial blurred image and the depth image with empty holes. The hidden node variables constitute the required ground-truth depth image. Each pixel node can only affect and be affected by other nodes connected to it, which share the same edges as shown in this figure.

A. MRF Formulation

The energy of each pixel, $E(p, D(p))$ in Eq. (7) is defined to penalize the depth choice $D(p)$. It is affected by the difference between $D(p)$ and the refined depth value available in each iteration, which will be defined as *data cost*. In addition, the depth values in a small region are usually similar to one another; hence, we need to avoid a large depth difference between two neighbor pixels; this penalty is defined

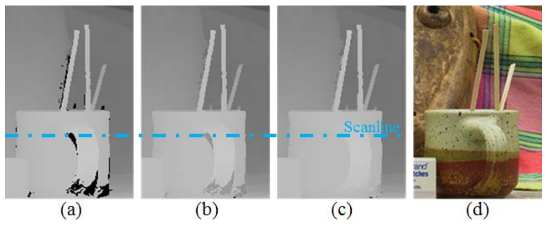

Fig. 6. Comparisons of depth filling results using our PatchMatch-based loopy belief propagation. (a) Input image with empty holes. (b) Filling result using depth values as labels directly. (c) Filling result using relative depth values as labels. (d) Color image reference. The scanline will be referred in Fig. 9.

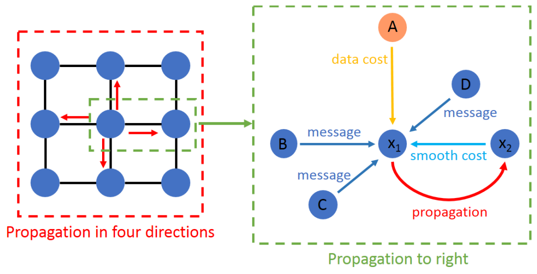

Fig. 7. Massage passing between pixel nodes. When passing a message from x_1 to x_2, we need to receive the message from the other three neighbor nodes B, C and D. Also, we need to get the data cost for node x_1 with label A.

as *smooth cost*. Thus, Eq. (7) can be defined as:

$$E(p, D(p)) = dataCost(p, D(p)) + \lambda * smoothCost(p, D(p)) \quad (8)$$

In order to get the data cost and smooth cost for pixel p with label $D(p)$ in Eq. (8), we need to define label $D(p)$ first. To make the optimization problem sufficiently efficient, our approach allows each node to have at most eight labels (candidates). The candidates are selected by PatchMatch approach. For each node p with unknown depth value $D(p)$, we let $P(p)$ be its corresponding patch with radius r in the intermediate deblurred result. Then, based on the implementation of [25] according to the authors' website at (http://www.ee.iisc.ac.in/labs/cvl/research/imdenoising), the N-nearest patches for $P(p)$ are obtained in the same color image. The depth label for patch $P(p)$ can be obtain in two ways. The first way is to use the evaluated depth value in the N-nearest patches as the label for $P(p)$. Depth evaluation for a candidate patch is performed by the sum-and-average approach as follows:

$$Depth(P'(p)) = \frac{\sum_{q \in P'(p)} D(q)}{\sum_{q \in P'(p)} isValid(q)} \quad (9)$$

where, $P'(p)$ is a candidate patch from the N-nearest patches for $P(p)$, $D(q)$ is the depth value of pixel q, and $isValid(q)$ is set to 1 if $D(q)$ is not equal to zero and set to 0 otherwise.

The disadvantage of the above method is that the evaluated depth of candidate patch $P'(p)$ directly used as labels for the missing depth values of $P(p)$ may cause inconsistency of depth intensities with neighbor depth values in depth map as shown in Fig. 6(b). This is because two patches with similar color information in the color image may be in two different depth layers of the depth map. We assume that the pixels in the same patch usually have similar depths, thus, we can use the relativity of depth information between two patches to adjust the evaluated depth by Eq. (9) as relative depth to be used as labels for missing depth of $P(p)$ in the depth image, and generate a depth label with a candidate patch $P'(p)$ as follows:

$$Label(p, P'(p)) = \frac{\sum_{q \in P(p), q' \in P'(p)} \frac{D(q)}{D(q')}}{\sum_{q \in P(p)} isValid(q)} \times Depth(P'(p)) \quad (10)$$

where, q' is the corresponding pixel that maps q from patch $P(p)$ to a candidate patch $P'(p)$. The result using relative depth is shown in Fig. 6(c), and empty holes are now filled with more smooth depth values for depth filling effects. And through applying the PatchMatch method, we can obtain eight nearest patches and generate eight labels as required. For each label from a candidate patch $P'(p)$, we use the data cost function to assign label $Label(p, P'(p))$ to node p as a penalty. The sum of absolute distances is used as the image distance in our approach. Thus, the data cost can be defined as:

$$dataCost(p, D(p)) = \sum_{q \in P(p), q' \in P'(p)} ||I(q) - I(q')|| \quad (11)$$

If we want to use color distance, then image I in Eq. (11) will be the intermediate deblur result. To use the depth distance, the refined depth image in each iteration is used instead. Experiments have shown that using the depth distance as the cost function can slightly improve the filling image in some regions; hence, it is used as the cost function in our approach.

In addition to the data cost, we use the smooth cost function to enforce local smoothing across adjacent nodes. Because we use MRF to solve the optimization problem, the smooth cost function for node p is only affected by its four immediate neighbor nodes, which we can defined as set $\theta(p)$. Thus, the smooth function can be defined by the depth difference as:

$$smoothCost(p, D(p)) = \sum_{q \in \theta(p)} ||Label(p, P'(p)) - D(q)|| \quad (12)$$

Next, we will show how to use loopy belief propagation to minimize the energy function by data cost and smooth cost.

B. Loopy Belief Propagation

Using PatchMatch to get the candidates, each node can have at most eight labels. Although eight candidates can improve the performance considerably compared to searching through all 255 choices for depths, minimizing Eq. (7) to get the exact solution remains a time-consuming task. Loopy belief propagation (LBP) is an efficient dynamic programming approach, which is commonly applied as energy minimization solution for Markov random fields [26]. We utilize LBP [27] to rapidly obtain an approximate solution. LBP is performed

Algorithm 1 Belief Propagation

```
1: BP($mrf, p, dir$)
2: for valid depth labels $i$ do
3:   for valid depth labels $j$ do
4:     $cost = dataCost(p, j) + smoothCost(i, j)$;
5:     for each direction $sDir$ except $dir$ do
6:       $cost += msg\{p_x, p_y\}.(sDir, j)$;
7:     end for
8:     $minCost$ = the minimum cost for all $j$;
9:   end for
10:  $newMsg(p_x, p_y, i) = minCost$;
11: end for
12: update $mrf$ with $newMsg$;
```

iteratively to converge to the final solution. In each iteration, a message is passed to adjacent nodes when all incoming messages have been received. In our method, there are four directions in total; hence, each pixel will receive a message from the other three directions before each propagation (See Fig. 7). We use a belief value array mrf to record message for each pixel, which is a four-dimensional matrix. Suppose we have a pixel $p = (p_x, p_y)$, the term $mrf\{p_x, p_y\}.(dir, d)$ denotes the belief value for pixel at position (p_x, p_y) with depth value d to its neighbor pixel in direction dir. Here, dir has four choices (up, down, right, and left), and the choices for d is equal to the maximum number of depth label candidates for each pixel. The belief propagation function $BP(mrf, p, dir)$ is called when we propagate the message of pixel p to the direction dir.

Algorithm 1 shows the details of this propagation function. Pixel p need to receive the message form the other three directions except dir. Pixels with different depth values will get different propagation messages. We use the minimum cost with neighbor pixels in the other three directions as the propagation message $newMsg(p_x, p_y, d)$ for pixel p with depth value d. The cost is obtained by the data cost, smooth cost, and belief values in the previous iteration, as shown in Algorithm 1. Then, the belief value array is updated with the new message. For example, if we propagate toward the right, then $mrf\{p_x + 1, p_y\}.(left, d) = newMsg(p_x, p_y, d)$. After propagation, the best candidate for each pixel is updated in function $MAP(mrf)$, which is done using Eq. (13). After all iterations, the best choice of depth value will be used to fill the empty areas:

$$best(p_x, p_y) = \arg\min_{d} \sum_{i} mrf\{p_x, p_y\}.(i, d) \tag{13}$$

We compared our initial depth filling results with the results of two other methods. The first method fills the empty areas using the nearest valid depth value on the same horizontal line. This method is fast and does not need any reference image. However, the filled result does not seem reasonable (See Fig. 8(b)). The other method performs depth filling by joint-bilateral filtering with the assistance of intermediate deblurred color images. The predicted depth value can be obtained by:

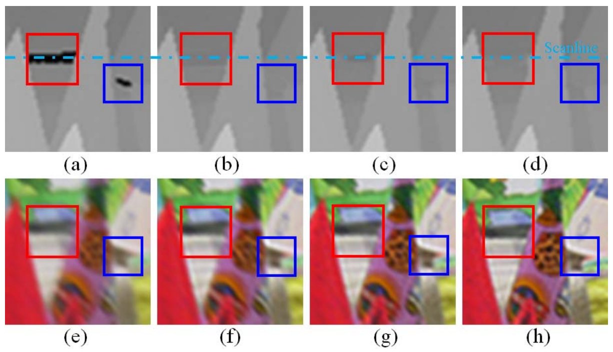

Fig. 8. Deblurring regarding depth hole filling. (a) Initial depth map with holes. (b) Depth map obtained by horizontal depth information. (c) Depth map filled by joint-bilateral filtering. (d) Our filled depth map using LBP-based initialization. (e) Input blurred image. (f) Deblurring using depth input (b). (g) Deblurring using depth input (c). (h) Deblurring result using depth input (d), and our depth filling results in high-quality deblurring. Note that improper depth filling will cause obvious ringing artifacts in the final deblurring results, especially in hole regions. Simple joint-bilateral filtering may address small hole (blue square in (c) and (g)), but it still causes problems in large hole regions (red square in (c) and (g)). The scanline will be referred in Fig. 9.

$$D_{fill}(p) = \frac{1}{W_p} \sum_{q\in\Omega(q)} G_s(||p-q||)G_r(||I(p)-I(q)||)D(q) \tag{14}$$

where, G_s is the spatial kernel, G_r is the range kernel, $I(q)$ is the color intensity of pixel q, $D(q)$ is the depth value, $\Omega(p)$ is the neighbor set of pixel p with valid depth values, and W_p is the normalizing weight term that is defined as:

$$W_p = \sum_{q\in\Omega(q)} G_s(||p-q||)G_r(||I(p) - I(q)||) \tag{15}$$

Joint-bilateral filtering (JBF) can restore empty areas consistently. However, for large empty holes, this method cannot predict the edges well (See Fig. 8(c)). Our filling result is shown in Fig. 8(d). Fig. 8(f)–(h) shows the deblurrling effects regarding hole fillings. It can be clearly seen from Fig. 8(f) that improper filling will cause deblurring artefacts, especially in hole regions. Fig. 8(g) shows that simply applying joint-bilateral filtering may address small hole, however, for relatively-large empty holes, this method cannot predict the edges well and may still cause problems in large hole regions for deblurring. Fig. 8(h) shows the deblurring method using our depth filling by LBP-based initialization, and our approach results in high-quality deblurring effects. Compared with Fig. 8(g), the improvement in deblurring for Fig. 8(h) is more pronounced in the whole neighboring region than just in the hole-region with depth filling by the LBP-based initialization. The reduction of the local errors in depth estimates will help improve the deblurring quality in each iteration, and the extent of the effects would improve on the deblurring in the whole neighboring region and globally (See the RMS error reduction for the “cones” scene in Table I).

We have also performed quantitative evaluations for the final deblurring results with different depth hole filling schemes. Table I shows the Root Mean Square (RMS) error comparison for deblurring results regarding different depth hole filling.

TABLE I
RMS ERROR COMPARISON FOR DEBLURRING REGARDING DEPTH FILLING

Method	art	books	bowling	cones	dolls	moebius
Initial Depth with Holes	11.6873	16.8564	6.7951	11.6458	23.7642	12.3513
Horizontal Depth Filling	10.2673	14.6952	6.3512	8.8962	21.3281	11.5383
JBF Depth Filling	9.7895	11.7134	5.9768	8.3529	12.6743	9.3372
LBP Depth Refinement	6.0058	5.3406	2.5775	6.7452	5.3989	3.9616

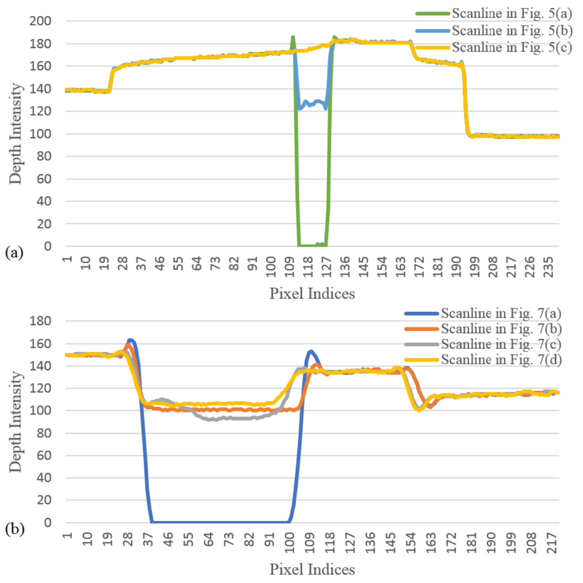

Fig. 9. Visualization of the 1D depth profiles. (a) The 1D depth profiles for the scanline in Fig. 6. (b) The 1D depth profiles for the scanline in Fig. 8.

We could see clearly from Table I that our LBP-based depth refinement is able to produce better deblurring results with the lowest RMS errors compared with other depth filling methods. Fig. 9(a) plots and visually compares the 1D depth profiles for the scanline in Fig. 6, and the 1D depth profile in Fig. 6(c) using relative depth values as labels shows best performance. Fig. 9(b) visually compares the 1D depth profiles for the scanline in Fig. 8, and the 1D depth profile in Fig. 8(d) shows best performance. The 1D depth profile in Fig. 8(c) is improper for the region of interest. Although the visualized 1D depth profile in Fig. 8(b) seems proper for the region of interest horizontally, yet it can be clearly seen from Fig. 8(b) that the depth values filled are obviously inconsistent vertically.

C. Depth Refinement

The LBP depth filling method described above is used to obtain the initial depth map with the blurred input as a reference. Because the intermediate deblurring results will improve as the number of deblurring iterations increases, our method uses intermediate results as references to refine the depth map. Our refining method is based on joint/cross bilateral filtering, the basic idea is shown in Eq. (14). The filtering is only implemented in areas that are empty in initial depth map. The two reference images used in joint/cross bilateral filtering are the intermediate result as the color reference and the LBP filling result as the depth reference. Our results indicate that the image quality of the depth map will improve with the quality enhancing of the color reference, as shown in Fig. 10.

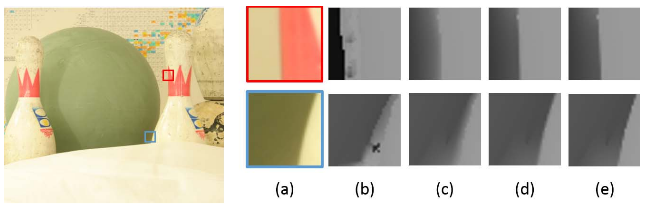

Fig. 10. Improvement by our depth refinement. (a) Clear color image. (b) Initial depth map by LBP depth filling. (c) Refined result using blurred image as color reference. (d) Refined result using intermediate deblurred results after 50 iterations as color reference. (e) Refined result using clear image as reference.

V. DEBLURRING MODEL

In this section, we illustrate our proposed depth-aware motion deblurring used in the deblurring process. We first introduce the Richardson-Lucy (RL) deconvolution method [6] and then show how to apply it to our model. The remainder of this section will describe the implementation details of our approach, including blurred image synthesis, regularization settings, and an extension for real captured images.

A. Proposed Deblurring Approach

Image blur occurs when an ideal point source does not appear as a point but spreads out into what we called a point-spread function (PSF). The information for each pixel is the sum of many individual point sources. Using PSF and the latent image, we can express pixel p in the blurred image using a convolution process as:

$$I_b(p) = c(p) = \sum_{q \in K} K_{pq} I(q) \tag{16}$$

where, I_b is the observed blur image and I is the latent clear image. p and q represent the pixel positions. $c(p)$ is a convolution process for a pixel located at p. K is the point spread function and K_{pq} represents the contribution of pixel q in the latent image to pixel p in the observed blurred image. Shepp and Vardi [28] have shown that we could use the likelihood probability for the Poisson distribution $P(I_b, K|I) = \prod_{q \in I} \frac{c(q)^{I_b(q)} e^{-c(q)}}{I_b(q)!}$ to model the Richardson-Lucy method as a maximum likelihood solution, and $c(q)$ is a convolution process for a pixel located at q. As the matrix of the second derivatives of $P(I_b, K|I)$ is negative semidefinite, it is a concave function [28]. For the optimization of $P(I_b, K|I)$, we follow [29, Th. 2.19(e)], and the Karush-Kuhn-Tucker conditions are the sufficient conditions for I to be a maximizer. For all $q \in I$, we deduce the iterative update rule for the Richardson-Lucy method as:

$$I(q) \frac{\partial}{\partial I(q)} ln(\prod_{q \in I} \frac{c(q)^{I_b(q)} e^{-c(q)}}{I_b(q)!}) = 0$$

$$I(q) \sum_{q \in I} \frac{\partial}{\partial I(q)} (I_b(q) ln(c(q)) - c(q) - ln(I_b(q)!)) = 0$$

$$I(q) \sum_{q \in I} \frac{I_b(q)}{c(q)} \frac{\partial}{\partial I(q)} c(q) - I(q) \sum_{q \in I} \frac{\partial}{\partial I(q)} c(q) = 0$$

$$I(q) \sum_{p \in K} \frac{I_b(p)}{c(p)} K_{pq} - I(q) \sum_{p \in K} K_{pq} = 0$$

Deblurring aims to calculate the most likely I given I_b and K. Since $\sum_{p \in K} K_{pq} = 1$, by adding the iteration index t and using Eq. (16), we could then obtain Eq. (17) and iteratively determine the pixel value for $I(q)$ as:

$$I(q)^{t+1} = I(q)^t \sum_{p \in K} \frac{I_b(p)}{I_b^t(p)} K_{pq} \tag{17}$$

where,

$$I_b^t(p) = \sum_{q \in K} K_{pq} I^t(q) \tag{18}$$

If we assume that the point-spread functions are the same for all the pixels, then Eq. (16) can be expressed in convolution form as shown in Eq. (6). Using convolution representation, we can transform Eq. (17) into Eq. (19) for the Richard-Lucy deconvolution as:

$$I^{t+1} = I^t \times K \otimes \frac{I_b}{I^t \otimes K} \tag{19}$$

To achieve pixel-level spatially variant blur, our motion blur model uses the matrix form for the blurred image, as shown in Eq. (5). Because the convolution form and the matrix form attempt to represent the same blurred image I_b given the clear image I, we hence have:

$$I^t(p) \otimes K = \frac{1}{n} \sum_{i=1}^{n} I^t(M_i p) \tag{20}$$

where, $I^t(p) \otimes K$ denotes the pixel value at position p for the convolution form. Now, we use another image, i.e., the error image I_e^t to show the error between the convolution result $I^t \otimes K$ and the blurred image I_b. We set I_e as:

$$I_e^t = \frac{I_b}{I^t \otimes K} = \frac{I_b}{\frac{1}{n}\sum_{i=1}^{n} I^t(M_i)} \tag{21}$$

Then, Eq. (19) can be applied for matrix form deblurring:

$$I^{t+1} = I^t \times K \otimes I_e^t = I^t \times \frac{1}{n} \sum_{i=1}^{n} M_i^{-1} I_e^t \tag{22}$$

Now we have transform convolution Richardson-Lucy method Eq. (19) into the matrix form Eq. (22). Hence, convolution is no longer needed. We also note that transformation matrix M_i is used only for matrix multiplication in the entire process. If we use a two-dimensional coordinate (p_x, p_y) for the pixel position, then M will be a 3×3 matrix. Now, when we add the depth value $D(p_x, p_y)$ to make the pixel position a three-dimensional vector (p_x, p_y, p_z), where $p_z = D(p_x, p_y)$, the deblurring process given by Eq. (22) is also valid once we use 4×4 transformation matrices M instead.

B. Blurring Synthesis and Deblurring

Given the clear image and its corresponding depth image, we can set the coordinate for each pixel as (p_x, p_y, p_z), where p_x and p_y are the pixel position in the clear image and p_z is the depth value in depth image. Then, we prepare several transformation matrices M, of which 16 are sufficient to translate the initial image into several frames. By summing and averaging each frame, we can obtain the synthesis results,

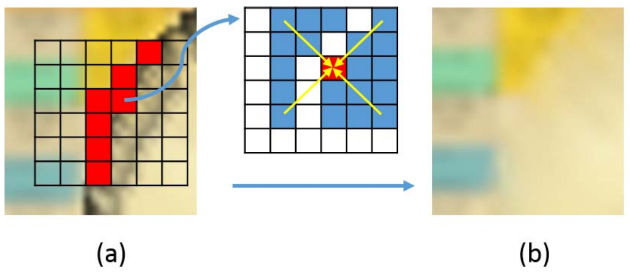

Fig. 11. Interpolation for blurred image synthesis. (a) Result synthesized directly from depth image. (b) Result of blur synthesis after interpolation. The empty areas (black areas) in (a) are fixed in (b).

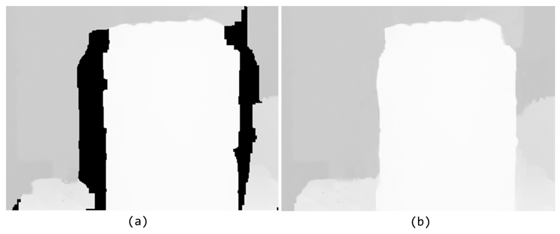

Fig. 12. Our depth filling (b) for real captured depth map after UV map (a).

which suffer from the problem of information loss as shown in Fig. 11(a). We can see from Fig. 11(a) that there are some black holes in the image, which means that there is no corresponding information for these areas. This is because we only have the depth value for the pixels in each frame. We cannot determine all the scene details in the entire 3D space. We can fill the empty holes using interpolation:

$$I(p) = \frac{\sum_{q \in \Omega(p)} w(q) I(q)}{\sum_{q \in \Omega(p)} w(q)} \tag{23}$$

where, $\Omega(p)$ is the set for valid pixels in the neighbor region of pixel p, and $w(q)$ is the weight for pixel q, $I(p)$ and $I(q)$ are their intensity values. The filling result is shown in Fig. 11(b). With the synthesis result and the transformation matrices M, we can now apply Eq. (22) to carry out the deblurring.

C. Regularization and Depth Updating

Noise is inevitable in real captured photos. To smooth out the noise in the blurred images, we use the total variation (TV) regularization term introduced in [5], [8], and [30] in order to suppress the image noise when performing deblurring. We define $P(I)$ as the prior probability of the recovered image I. Therefore, we have the optimization function as:

$$\begin{aligned} \arg\max_I P(I|I_b, K) &= \arg\max_I P(I_b, K|I)P(I) \\ &= \arg\min_I -ln(P(I_b, K|I)) - ln(P(I)) \\ &= \arg\min_I \sum_{q \in I} (c(q) - I_b(q) ln(c(q)) \\ &\quad + \lambda R(I(q))) \end{aligned} \tag{24}$$

where, $R(I) = -\frac{1}{\lambda} ln(P(I))$ is the regularization term used, and λ is the weight for the regularization. We calculate the first derivative for Eq. (24) according to $I(q)$ and let it equal

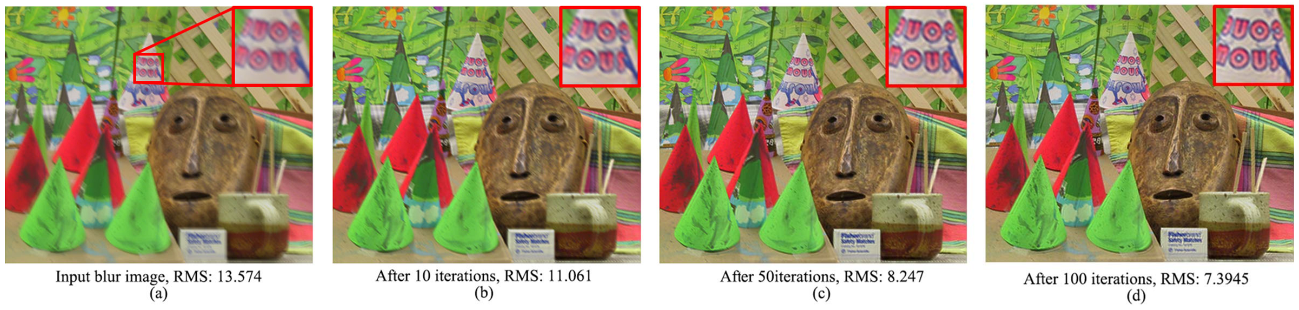
Input blur image, RMS: 13.574
(a)
After 10 iterations, RMS: 11.061
(b)
After 50iterations, RMS: 8.247
(c)
After 100 iterations, RMS: 7.3945
(d)

Fig. 13. Decrease in RMS errors with increase in number of iterations. (a) Input blurred image. (b)–(d) Deblurring results after different numbers of iterations.

to 0, we hence have the following equation as:

$$\sum_{p\in K}\frac{I_b(p)}{\sum_{q\in K}K_{pq}I^t(q)}K_{pq}=1-\lambda\nabla R(I(q))) \tag{25}$$

where, $\nabla R(I(q))$ is the first derivative of $R(I(q))$. As $t\rightarrow\infty$, we want to make the Richardson-Lucy method get convergence, I^{t+1}/I^t should equal to 1. Thus, using Eq. (25), the regularized Richardson-Lucy method could be expressed as:

$$I^{t+1}(q)=\frac{I^t(q)}{1-\lambda\nabla R(I^t(q))}\sum_{p\in K}\frac{I_b(p)}{\sum_{q\in K}K_{pq}I^t(q)}K_{pq} \tag{26}$$

with its convolution representation as:

$$I^{t+1}=\frac{I^t}{1-\lambda\nabla R(I^t)}\times K\otimes\frac{I_b}{I^t\otimes K} \tag{27}$$

Similarly, as shown in Section V-A, we could obtain the new regularized form using Eq. (26) as:

$$I^{t+1}=\frac{I^t}{1-\lambda\nabla R(I^t)}\times\frac{1}{n}\sum_{i=1}^{n}M_i^{-1}I_e^t \tag{28}$$

The total variation (TV) regularization in [5], [8], and [30] is then applied for suppress noise during the deblurring. By replacing the regularization term $\nabla R(I^t)$ in Eq. (28) with $\nabla R_{TV}(I^t)$, we could obtain Eq. (29) as following:

$$I^{t+1}=\frac{I^t}{1-\lambda\nabla R_{TV}(I^t)}\times\frac{1}{n}\sum_{i=1}^{n}M_i^{-1}I_e^t \tag{29}$$

where,

$$\nabla R_{TV}(I^t)=-\nabla\frac{\nabla I^t}{|\nabla I^t|} \tag{30}$$

The solution introduced in [5] initializes λ as 1.0, and decreases it after every 100 iterations. However, in our experiments, we will restart the iterative procedure each time we update the depth image. Hence, we set λ to a small fixed value between 0.0001 to 0.001 (with image intensity varying from 0 to 1.0). In the depth filling process, the quality of the reference color image will affect the filled results. Hence, starting with the blurred image, we update the reference color image after a fixed number of iterations each time. In most cases, the iteration number will be set to 10. We do not update the reference image after each deblurring iteration because there is only a slight difference between two neighbor intermediate results. Frequent updating will be a time-consuming task.

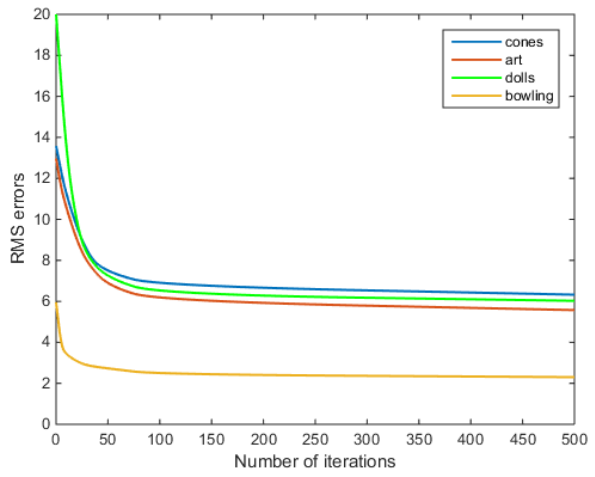

Fig. 14. Convergence of RMS errors with the increasing of iteration numbers for four different images: “cones”, “art”, “dolls” and “bowling”.

D. Real Case Deblurring

In blurring synthesis, we decompose the blur kernel into several motion trajectories. Since the blur kernels in the real-life cases may have inconstant values, the decomposed trajectories might have different weights accordingly. However, in this paper, for problem simplicity, we utilize uniform motion assumption, which means the trajectories in this paper have the same weight. We have our transformation matrix $M_i=H_iP$, where $H_i=\prod_{j=1}^{i}h_j$. With the uniform motion assumption, all the trajectories in the paper will have the same weight, namely, $h_1=h_2=\cdots=h_i$. Thus, $h_j=\sqrt[i]{H_i}$, $1\leq j\leq i$. Therefore, we can obtain h_j through calculating the ith matrix root of H_i [31], and estimation for the series of h_j is reduced to the estimation of H_i. Although our approach is a non-blind deblurring method, it can be extended to images captured by 3D cameras. The additional task required for real case deblurring is motion estimation, which is essential for transformation matrix construction. In this study, motion estimation is performed with user assistance, which gives the positions of pixel pairs before and after motion. Suppose that the position set for pixels before motion is defined as B and that for pixels after motion is defined as A. Obviously, A is the result of B multiplied by the transformation matrix M. Hence, we can obtain the transformation matrix M by:

$$M=B^{-1}A \tag{31}$$

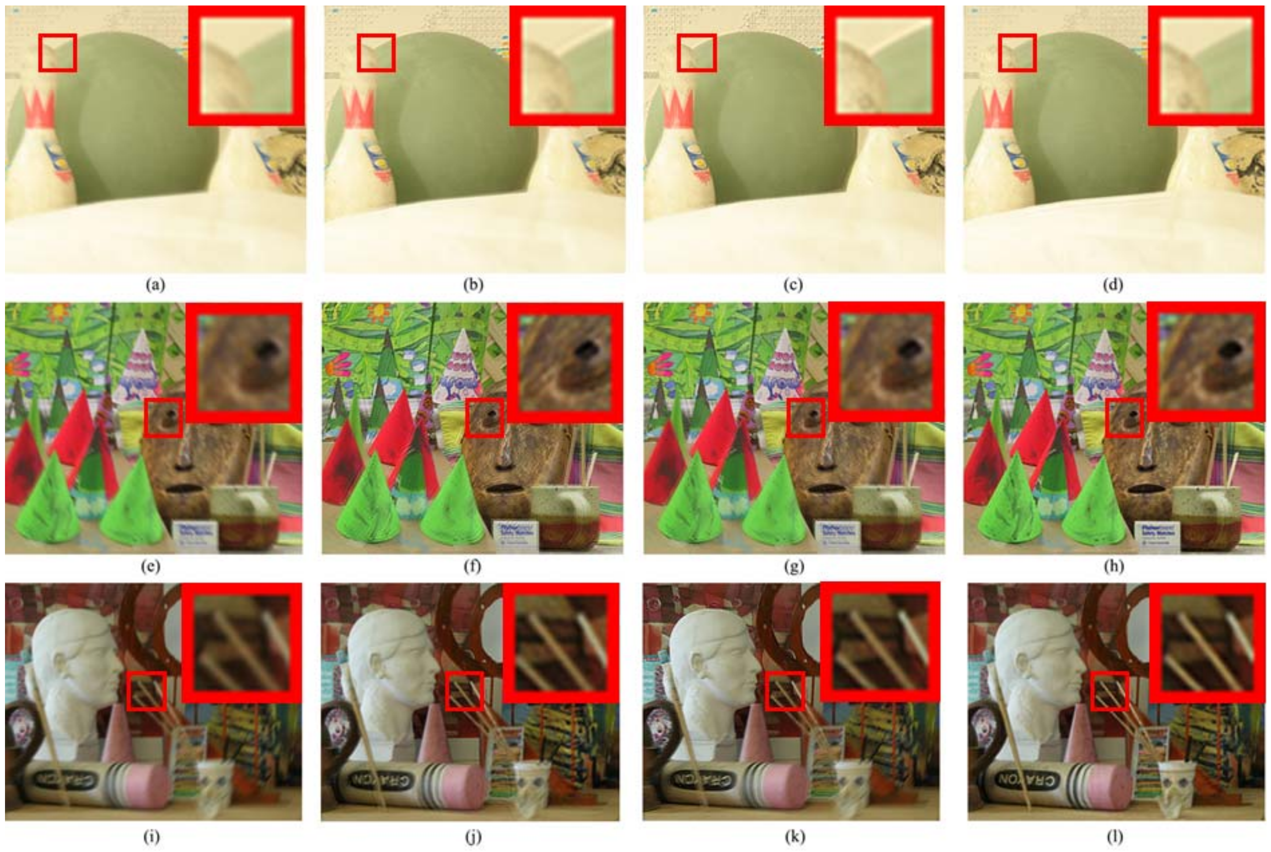

Fig. 15. Comparison of deblurring results of our method with those of two other methods. The first column is the input blurred image. The second column shows the results of [5]. The third column shows the results of [13]. The final column shows our results.

The total motion will then be divided into n sub-motions represented by n transformation matrices. In our approach, we divided the motion into n parts. These n sub-matrices are then used to perform the deblurring as shown in Eq. (22). Because some empty holes remain in the depth map, the depth filling and depth refinement phases in our framework are still necessary. Fig. 12 shows the improvement achieved after our depth filling approach is applied to a real captured depth map.

VI. Experimental Results

This section presents our experimental results, and the images we used are all obtained from the Middlebury stereo datasets (http://vision.middlebury.edu/stereo). RMS error analysis showed that our method would converge as the number of iterations increases. Comparisons between our method and other methods proved that our method could handle scenes with large depth differences. Moreover, we tested our method with noisy blurred images to demonstrate its robustness.

A. Convergence Analysis

Both the RL algorithm and the method introduced in [5] have been shown to be convergent. We tested our method in the same way to observe the changes in the RMS errors after each iteration. Because the number of iterations was large in the experiment, we updated the filled depth image every 10 iterations only over the first 100 iterations. Subsequently, this updating procedure would be repeated after every 100 iterations (instead of 10). The parameter λ was set to 0.0005 (color intensity varying from 0 to 1.0) for the regularization term in this example for all the iterations. Fig. 13(b)–(d) shows the deblurring results after different numbers of iterations. We defined the updating rate according to the similarity between two neighbor intermediate results. Fig. 14 shows the convergence of the RMS errors for four images with different levels of blur. We can see that the RMS decreases rapidly in the first 50 iterations. Most cases converge within 500 iterations according to our experiments. Moreover, the difference in the deblurring results is negligible after 100 iterations for images that are not blurred severely. We have performed the convergence analysis on an Intel® Core^{TM} 4.00GHz CPU with 8GB memory over an image at the resolution of 1390×1110 from the Middlebury datasets. We have performed our depth-aware deblurring for 1000 times to obtain the more meaningful average convergence time for stable purpose. Table II shows the running time of our convergence analysis. According to Table II, the whole convergence process costs about 36.04 seconds. Other operations including pre-processing and post-processing only take 0.23 seconds. Therefore, our method takes 36.27 seconds in total to obtain the final deblurring, which achieves high-quality deblurring at favorable speed.

TABLE II
RUNNING TIME OF OUR CONVERGENCE ANALYSIS

	1st 10 iters	2nd 10 iters	3rd 10 iters	4th 10 iters	5th 10 iters
Depth Map	5.89s	4.71s	3.23s	2.78s	2.16s
Deblurring	4.32s	3.88s	2.18s	2.13s	1.18s
Total	10.21s	8.59s	5.41s	4.91s	3.34s
	6th 10 iters	7th 10 iters	8th 10 iters	9th 10 iters	10th 10 iters
Depth Map	0.94s	0.54s	0.38s	0.15s	0.07s
Deblurring	0.85s	0.34s	0.21s	0.06s	0.04s
Total	1.79s	0.88s	0.59s	0.21s	0.11s

B. Comparison With State-of-the-Art Methods

In this section, we will illustrate the difference between our approach and other deblurring methods. First, we compare our approach with the methods introduced in [5] and [13]. The former employs a deblurring model that is nearly the same as ours. Hence, transformation matrices are also used in their method, except the data for depth. We set the depth to 0.5 (with maximum depth value equal to 1.0) to simulate their results. Further, we used the total variant regularization term with λ set to 0.0005 for both methods. The work of [13] is a blind deblurring method. Hence, we used our synthesized blurred image as the input, and the deblurring results were obtained using the software provided on their website with the default setting in CPU mode.

Fig. 15 shows the deblurring results of the three methods, with enlarged details for comparison. The first row is for the scene "bowling" scene, which suffers from large depth difference. While in the second row, i.e. the "cones" scene, the depth range is rather small. Finally, in the third row, i.e. the "art" scene, image blur is caused by rotation around the top-left corner. Compared to the blurring input in the first column, the results of [5] (second column) and the results of [13] (the third column) indicate better performance at the center of the scene. However, the background of the scene is over-deblurred for these two methods, resulting in some "white" pixels and areas in the background. In addition, the foreground regions lack deblurring, leading to obvious ringing artefacts. This is because the method introduced in [13] cannot handle spatially variant blurring. Hence, the entire image is deblurred with the same kernel estimated from the blurred image. Although the method introduced in [5] can handle spatially variant PSFs without considering depth information, it can only deal with this problem in two-dimensional image spaces. Thus, the inner and outer parts of the image will be deblurred in different ways. However, objects near to and far away from camera will not produce different results in the case of this method [5]. Our results are shown in the last column, and they indicate that both near and far areas in the scene are deblurred with higher visual quality, with fewer ringing artefacts in foreground and a clear, accurate background.

Fig. 16 shows the RMS errors of these methods in the three scenes: "cones", "bowling" and "art". The results of the method introduced in [13] indicate failure for the "bowling" and "art" scenes, with RMS errors greater than the input image. The results of the method introduced in [5] indicate failure for the "bowling" scene. The depth range in the "bowling" scene is large; hence, without depth information, these two methods [5], [13] cannot process the foreground and background differently and effectively. The blurriness in the "art" scene is caused by rotation, which is difficult for the method introduced in [13] to handle. However, our approach avoids such problems by considering the depth information and refining the depth maps during the deblurring processes.

We further compare our approach with three other kernel-based spatially invariant non-blind deblurring methods, namely RL deconvolution [6], the method of Shan *et al.* [10], and the method of Xu and Jia [32], in order to show the advantages of our motion blur model. Since our model is matrix-based, we need to generate a blur kernel from our transformation matrices. Fig. 17 shows the kernel estimated details. We select

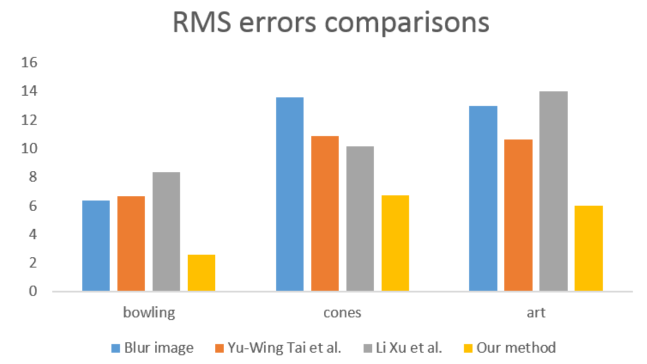

Fig. 16. RMS errors comparison of our results with the results of Tai *et al.* [5] and Xu *et al.* [13]. The images used are "bowling", "cones", and "art".

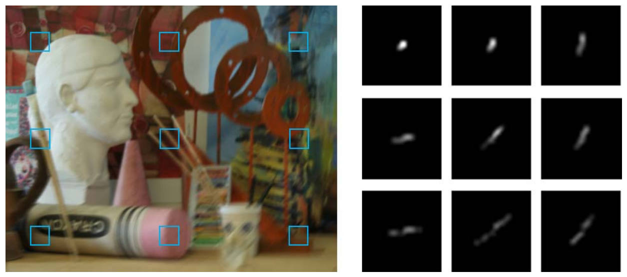

Fig. 17. Nine kernels estimated from blur images synthesized by our blur model (rotation around the top-left corner). We selected nine different positions in the image and generate point spread functions for these pixels.

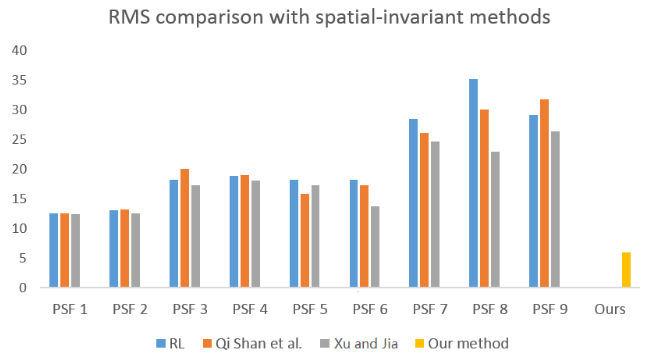

Fig. 18. RMS error comparison between our approach and three other spatial-invariant deblurring methods: RL deconvolution [6], Shan *et al.* [10] and Xu and Jia [32]. The nine PSFs used for the three methods are shown in Fig. 17.

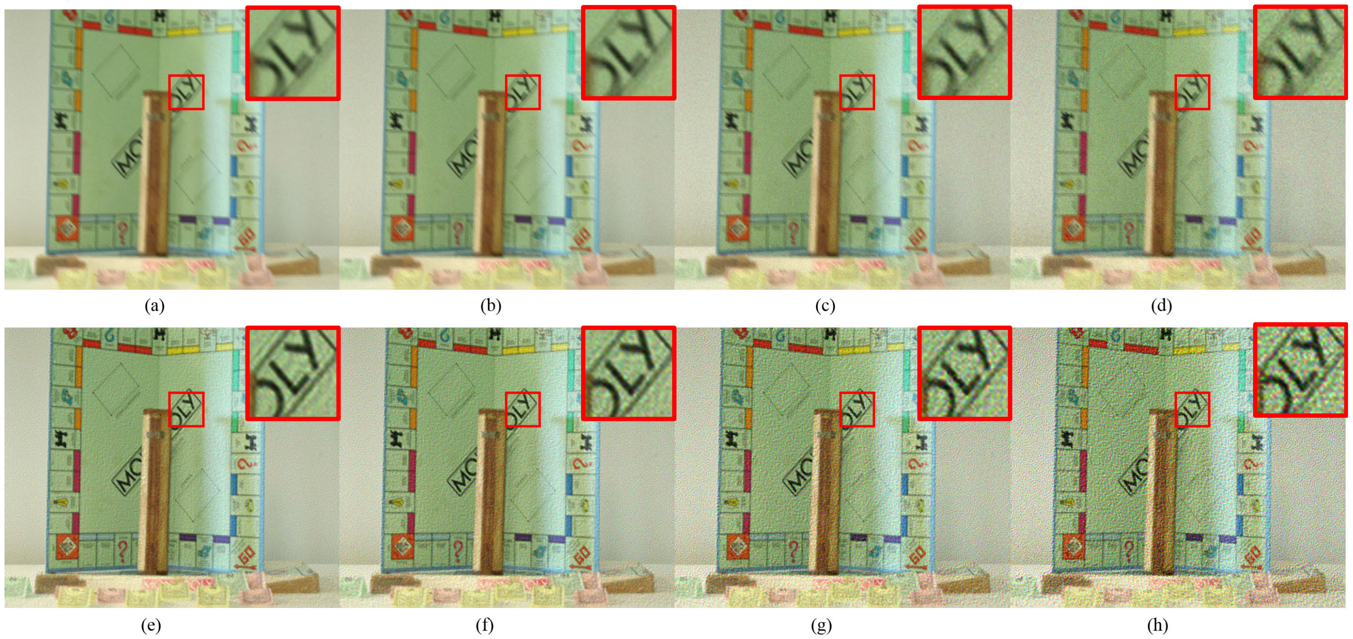

Fig. 19. Noisy images deblurring. The top row shows the noisy input blurred images. The second row shows our deblurred results. Gaussian noise is used with u set to 0 and σ set to 0.0002, 0.0004, 0.001, and 0.002 from left to right. RMS errors with the ground-truth clear images are given below each image.

nine positions in the image (left part of Fig. 17), and use the blur kernels of these nine pixels (right part of Fig. 17) as the kernel candidates. Then, we tested all nine kernels using the three spatially invariant deblurring methods. Fig. 18 shows the RMS errors of the three methods with the nine kernels given for the "art" scene under rotational motion (rotation around the top-left corner). Our approach is a spatially variant version that uses matrix transformation with a unique RMS error given on the right. The results show that our method produces a much lower RMS error than the three methods [6], [10], [32].

C. Noisy and Over-Blurred Images

We estimated the robustness of our approach by testing it on noisy images. We use the *imnoise* function in Matlab to add noise to our synthesized blurred images before deblurring. Gaussian noise was used in our experiment with a mean value of 0. The first row in Fig. 19 shows the noisy blur images with σ set to 0.0002, 0.0004, 0.001, and 0.002 respectively. Our deblurring results are shown in the second row. From the RMS errors, we can see that our method can handle low noise levels well and produces results with lower RMS errors than input noisy image. For noise with large σ, our method does not amplify noise significantly, and the deblurring results remain reasonable. We also tested our approach with over-blurred image. However, for largely over-blurred cases as shown in Fig. 20(a), where the blur information is too complicated, our approach may not be able to fully recover a perfect deblurring and results in a failure case as shown in Fig. 20(b). But to some extent, the deblurred result Fig. 20(b) is still more visually pleasing than the original blurred image, which also means our depth-aware motion deblurring requires further development and more future work for further enhancement.

D. Real Examples

We use Intel® RealSense™ 3D Camera F200 to capture both the color and the depth image for real case deblurring. The RealSense™ Camera F200 is a stand-alone camera that can be attached to a computer, and can be applied for natural gesture interaction, face recognition, 3D scanning, etc. It contains mainly three key components, namely, a conventional camera, an infrared laser projector, and an infrared camera [33]. The infrared projector projects a grid onto the scene, and the infrared camera captures it to obtain depth maps. The RealSense™ Camera F200 has an effective range between 0.2m and 1.2m; the color camera supports resolution up to 1080p at 30FPS and 720p at 60FPS; the depth (infrared) camera supports depth resolution up to 480p at 60FPS and HVGA quality at 110FPS, and supports infrared resolution up to 480p at 300FPS [33]. Therefore, there is no need for capturing the depth maps separately using a tripod or other methods. The depth map capturing speed by RealSense™ Camera F200 is much faster than the capturing speed for the corresponding color image. In this way, utilizing a at least less blurred depth map as supplemental information for helping deblurring the more blurred color image is meaningful and would help promote the deblurring quality. Also, our work mainly focuses on depth-aware motion deblurring using loopy belief propagation, while the motion-blurred color images and the related clear depth maps are obtained using RealSense™ Camera F200. We used the UV maps provided in the SDK to map the depth map to the coordinates of the color image.

Real examples usually have complicated motions such as zoom-in (zoom-out) or rotation. Motion estimation for real captured images was performed with pixels pairs provided by users as shown in Fig. 21(a). Based on uniform motion assumption, easiest way to handle such uniform motion is

TABLE III
RMS ERROR COMPARISON FOR DEBLURRING RESULTS WITH RESPECT TO THE NUMBER OF PIXEL PAIRS FOR USER-ASSISTED MARKUPS

Markups	art	books	bowling	cones	dolls	moebius
Blur Image	12.9739	17.5476	6.3319	13.5744	26.3987	13.3389
2 Pairs	12.1456	16.9376	6.1532	12.7369	24.4268	12.8394
4 Pairs	10.3528	13.3572	5.8527	10.3418	18.3712	10.6315
6 Pairs	8.7214	9.8693	4.8672	8.1385	11.7364	8.3571
8 Pairs	6.8972	6.0617	2.5875	7.1273	6.3247	4.4361
10 Pairs	6.3214	5.1131	2.4952	6.8317	5.6247	4.2136

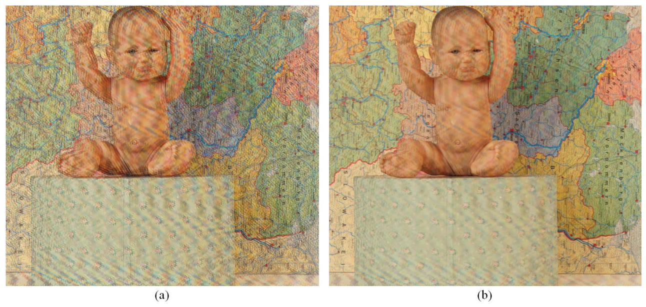

Fig. 20. Failure case from too over-blurred image. (a) Largely over-blurred image. (b) Failure case from our approach. Although the deblurring result is visually better than the over-blurred input, yet we still need to perform more further researches on our approach to provide better deblurring effects.

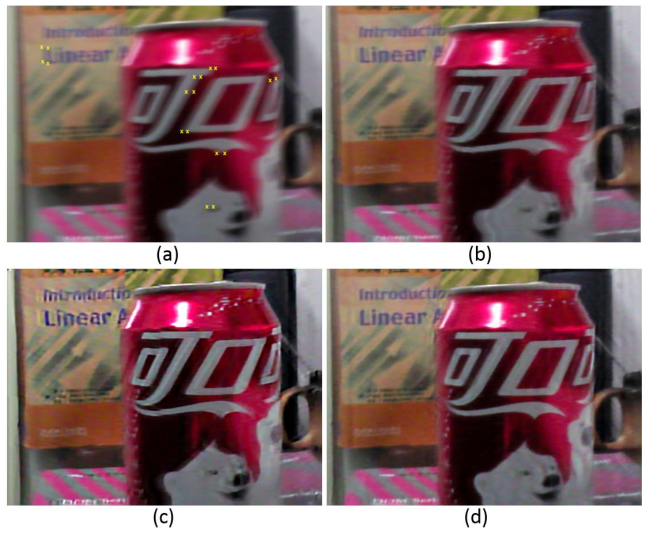

Fig. 21. Comparison of results for real captured images. (a) Input blurred image with user-assisted markups of pixel pairs for motion estimation. (b) Result by [5]. (c) Result by [13]. (d) Our result.

presented by Shan *et al.* [34]. Their method relies on user to provide image correspondences to build the transformation in deblurring. Dai and Wu [35] also presented an effective method to estimate H_i by blurred objects alpha matte. We utilize the method in [34] for real example experiments. Li *et al.* [36] further introduced sharp panoramas generation from motion-blurred videos, the method for estimating a global homography could also be applied as motion path estimation in this paper. In Fig. 21, transformation matrix M_i is obtained by fitting the transformation matrix with user-assisted markups of pixel pairs. Each h_j is calculated under uniform motion assumption. We compared our result (Fig. 21(d)) with [5] (Fig. 21(b)) and [13] (Fig. 21(c)). As can be seen from the results, without depth consideration, background was over-deblurred in Fig. 21(b). Our approach worked well for both the near and far areas. We note that our real example is not as perfect and significant as synthetic examples, which is mainly caused by estimation errors for h_j. Besides, motions in our real example are also not as huge as in synthesized blurred images. To evaluate the accuracy relation between user interaction and final deblurring results, we have performed quantitative evaluations on the synthetic examples with user-assisted markups of pixel pairs. Table III shows the Root Mean Square (RMS) error comparison for deblurring results with respect to the number of pixel pairs for user-assisted markups. It can be seen clearly from Table III that, by increasing the number of user-assisted pixel pairs, the RMS error reduces accordingly, and more than eight pairs of correspondence points could produce high-quality deblurring results.

VII. CONCLUSION AND FUTURE WORK

It is difficult to restore a spatially variant blurred image, especially when each pixel has an individual point-spread function. Moreover, existing studies have not paid sufficient attentions to the differences in blurriness caused by varying depth values. To address such issues, this paper proposes a matrix-based motion blur model to synthesize a blurred image with pixel-level spatially variant blur by using a depth image. We applied several transformation matrices using the 3D space and slice motion to produce intermediate frames and summed them up to form the blurred image. The problems of empty holes that occur in most depth images are fixed through our depth filling approach. We also propose an iterative approach to restore latent clear images using our blur model. The experimental results showed that our model can simulate image blur caused by three-dimensional motion, and the deblurring results are robust in different depth layers.

In the future, based on the model in this research, we will further work on image/video deblurring with nonuniform motion velocity assumption [37], [38]. We will further study and work on jointly optimizing the depth map [39]–[41] and clear image for the benefits of blur kernel estimation [37], [42] to propose a more general solution to handle blind image deconvolution. We also plan to improve depth filling quality for objects' edges in order to make them sharper and more consistent with color reference images. Motion animation for real captured images is another important task, which would be fully automated and hence more effective than user assistance.

REFERENCES

[1] A. Levin, "Blind motion deblurring using image statistics," in *Proc. IEEE 19th Int. Conf. Neural Inf. Process. Syst.*, Dec. 2006, pp. 841–848.

[2] J. Bardsley, S. Jefferies, J. Nagy, and R. Plemmons, "Blind iterative restoration of images with spatially-varying blur," *Opt. Express*, vol. 14, no. 5, pp. 1767–1782, 2006.

[3] S. Cho, Y. Matsushita, and S. Lee, "Removing non-uniform motion blur from images," in *Proc. IEEE 11th Int. Conf. Comput. Vis.*, Oct. 2007, pp. 1–8.

[4] F. Li, J. Yu, and J. Chai, “A hybrid camera for motion deblurring and depth map super-resolution,” in *Proc. IEEE Conf. Comput. Vis. Pattern Recognit.*, Jun. 2008, pp. 1–8.

[5] Y.-W. Tai, P. Tan, and M. S. Brown, “Richardson-Lucy deblurring for scenes under a projective motion path,” *IEEE Trans. Pattern Anal. Mach. Intell.*, vol. 33, no. 8, pp. 1603–1618, Aug. 2011.

[6] W. H. Richardson, “Bayesian-based iterative method of image restoration,” *J. Opt. Soc. Amer.*, vol. 62, no. 1, pp. 55–59, 1972.

[7] N. Wiener, *Extrapolation, Interpolation, and Smoothing of Stationary Time Series*. Cambridge, MA, USA: MIT Press, 1964.

[8] T. F. Chan and C.-K. Wong, “Total variation blind deconvolution,” *IEEE Trans. Image Process.*, vol. 7, no. 3, pp. 370–375, Mar. 1998.

[9] A. Levin, R. Fergus, F. Durand, and W. T. Freeman, “Image and depth from a conventional camera with a coded aperture,” *ACM Trans. Graph.*, vol. 26, no. 3, p. 70, 2007.

[10] Q. Shan, J. Jia, and A. Agarwala, “High-quality motion deblurring from a single image,” *ACM Trans. Graph.*, vol. 27, no. 3, p. 73, 2008.

[11] A. Levin, Y. Weiss, F. Durand, and W. T. Freeman, “Understanding and evaluating blind deconvolution algorithms,” in *Proc. IEEE Conf. Comput. Vis. Pattern Recognit.*, Jun. 2009, pp. 1964–1971.

[12] J. Jia, “Single image motion deblurring using transparency,” in *Proc. IEEE Conf. Comput. Vis. Pattern Recognit.*, Jun. 2007, pp. 1–8.

[13] L. Xu, S. Zheng, and J. Jia, “Unnatural L0 sparse representation for natural image deblurring,” in *Proc. IEEE Conf. Comput. Vis. Pattern Recognit.*, Jun. 2013, pp. 1107–1114.

[14] D. Krishnan and R. Fergus, “Fast image deconvolution using hyper-laplacian priors,” in *Proc. NIPS*, 2009, pp. 1033–1041.

[15] P. Meer, “Robust techniques for computer vision,” in *Emerging Topics in Computer Vision*, G. Medioni, and S. B. Kang, Eds. Upper Saddle River, NJ, USA: Prentice-Hall, 2004, ch. 4, pp. 109–190.

[16] L. Yuan, J. Sun, L. Quan, and H.-Y. Shum, “Image deblurring with blurred/noisy image pairs,” *ACM Trans. Graph.*, vol. 26, no. 3, p. 1, Jul. 2007.

[17] M. Ben-Ezra and S. K. Nayar, “Motion deblurring using hybrid imaging,” in *Proc. IEEE Comput. Soc. Conf. Comput. Vis. Pattern Recognit.*, Jun. 2003, p. 1.

[18] Y. Xu, X. Hu, and S. Peng, “Sharp image estimation from a depth-involved motion-blurred image,” *Neurocomputing*, vol. 171, pp. 1185–1192, Jan. 2016.

[19] J. Bardsley, S. Jefferies, J. Nagy, and R. Plemmons, “A computational method for the restoration of images with an unknown, spatially-varying blur,” *Opt. Exp.*, vol. 14, no. 5, pp. 1767–1782, 2006.

[20] Y.-W. Tai, H. Du, M. S. Brown, and S. Lin, “Correction of spatially varying image and video motion blur using a hybrid camera,” *IEEE Trans. Pattern Anal. Mach. Intell.*, vol. 32, no. 6, pp. 1012–1028, Jun. 2010.

[21] C. J. Schuler, M. Hirsch, S. Harmeling, and B. Schölkopf, “Learning to deblur,” *IEEE Trans. Pattern Anal. Mach. Intell.*, vol. 38, no. 7, pp. 1439–1451, Jul. 2016.

[22] N. Kumar, R. Nallamothu, and A. Sethi, “Neural network based image deblurring,” in *Proc. IEEE Symp. Neural Netw. Appl. Elect. Eng.*, Sep. 2012, pp. 219–222.

[23] L. Xu and J. Jia, “Depth-aware motion deblurring,” in *Proc. IEEE Int. Conf. Comput. Photogr.*, Apr. 2012, pp. 1–8.

[24] T. Akenine-Möller, E. Haines, N. Hoffman,A. Pesce, M. Iwanicki, and S. Hillaire, *Real-Time Rendering*. Natick, MA, USA: CRC Press, 2018.

[25] S. M. Haque, G. P. Pai, and V. M. Govindu, “Symmetric smoothing filters from global consistency constraints,” *IEEE Trans. Image Process.*, vol. 24, no. 5, pp. 1536–1548, May 2015.

[26] R. Szeliski *et al.*, “A comparative study of energy minimization methods for Markov random fields with smoothness-based priors,” *IEEE Trans. Pattern Anal. Mach. Intell.*, vol. 30, no. 6, pp. 1068–1080, Jun. 2008.

[27] J. Pearl, “Reverend Bayes on inference engines: A distributed hierarchical approach,” in *Proc. IEEE Conf. Artif. Intell. AAAI*, Aug. 1982, pp. 133–136.

[28] L. A. Shepp and Y. Vardi, “Maximum likelihood reconstruction for emission tomography,” *IEEE Trans. Med. Imag.*, vol. MI-1, no. 2, pp. 113–122, Oct. 1982.

[29] Y. Vardi, *Nonlinear Programming*. Upper Saddle River, NJ, USA: Prentice-Hall, 1969.

[30] N. Dey and L. Blanc-Feraud, C. Zimmer, Z. Kam, J.-C. Olivo-Marin, and J. Zerubia, “A deconvolution method for confocal microscopy with total variation regularization,” in *Proc. IEEE Int. Symp. Biomed. Imag., Nano Macro*, Apr. 2004, pp. 1223–1226.

[31] D. A. Bini, N. J. Higham, and B. Meini, “Algorithms for the matrix pth root,” *Numer. Algorithms*, vol. 39, no. 4, pp. 349–378, 2005.

[32] L. Xu and J. Jia, “Two-phase kernel estimation for robust motion deblurring,” in *Proc. Eur. Conf. Comput. Vis.*, Sep. 2010, pp. 157–170.

[33] Intel. (2016). *Specifications for the Intel RealSense Camera F200*. [Online]. Available: https://communities.intel.com/docs/DOC-24012

[34] Q. Shan, W. Xiong, and J. Jia, “Rotational motion deblurring of a rigid object from a single image,” in *Proc. IEEE 11th Int. Conf. Comput. Vis.*, Oct. 2007, pp. 1–8.

[35] S. Dai and Y. Wu, “Motion from blur,” in *Proc. IEEE Conf. Comput. Vis. Pattern Recognit.*, Jun. 2008, pp. 1–8.

[36] Y. Li, S. B. Kang, N. Joshi, S. M. Seitz, and D. P. Huttenlocher, “Generating sharp panoramas from motion-blurred videos,” in *Proc. IEEE Conf. Comput. Vis. Pattern Recognit.*, Jun. 2010, pp. 2424–2431.

[37] L. Zhang, L. Zhou, and H. Huang, “Bundled kernels for nonuniform blind video deblurring,” *IEEE Trans. Circuits Syst. Video Technol.*, vol. 27, no. 9, pp. 1882–1894, Sep. 2017.

[38] C. Qiao, R. W. H. Lau, B. Sheng, B. Zhang, and E. Wu, “Temporal coherence-based deblurring using non-uniform motion optimization,” *IEEE Trans. Image Process.*, vol. 26, no. 10, pp. 4991–5004, Oct. 2017.

[39] Z. Jin, T. Tillo, W. Zou, Y. Zhao, and X. Li, “Robust plane detection using depth information from a consumer depth camera,” *IEEE Trans. Circuits Syst. Video Technol.*, vol. 29, no. 2, pp. 447–460, Feb. 2019.

[40] H. Yan, X. Yu, Y. Zhang, S. Zhang, X. Zhao, and L. Zhang, “Single image depth estimation with normal guided scale invariant deep convolutional fields,” *IEEE Trans. Circuits Syst. Video Technol.*, vol. 29, no. 1, pp. 80–92, Jan. 2019.

[41] B. Wang, J. Zou, Y. Li, K. Ju, H. Xiong, and Y. F. Zheng, “Sparse-to-dense depth estimation in videos via high-dimensional tensor voting,” *IEEE Trans. Circuits Syst. Video Technol.*, vol. 29, no. 1, pp. 68–79, Jan. 2019.

[42] S. Liu, H. Wang, J. Wang, and C. Pan, “Blur-kernel bound estimation from pyramid statistics,” *IEEE Trans. Circuits Syst. Video Technol.*, vol. 26, no. 5, pp. 1012–1016, May 2016.

Bin Sheng received the Ph.D. degree in computer science and engineering from The Chinese University of Hong Kong, Hong Kong, China. He is currently an Associate Professor with the Department of Computer Science and Engineering, Shanghai Jiao Tong University, Shanghai, China. His current research interests include image-based rendering, machine learning, virtual reality, and computer graphics.

Ping Li received the Ph.D. degree in computer science and engineering from The Chinese University of Hong Kong, Hong Kong, China. He is currently an Assistant Professor with the Macau University of Science and Technology, Macau, China. His current research interests include image/video stylization, big data visualization, GPU acceleration, and creative media. He has one image/video processing national invention patent and has excellent research project reported worldwide by *ACM TechNews*.

Xiaoxin Fang received the B.Eng. and the M.Eng. degrees in computer science from the Department of Computer Science and Engineering, Shanghai Jiao Tong University, Shanghai, China. His current research interests include image/video deblurring, real-time computer graphics, machine learning, and computer vision.

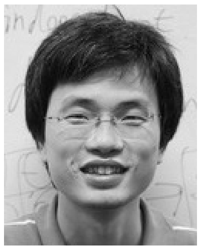

Ping Tan received the Ph.D. degree in computer science and engineering from the Hong Kong University of Science and Technology, Hong Kong, China. He is currently an Associate Professor with the School of Computing Science, Simon Fraser University, Burnaby, BC, Canada. His current research interests include computer vision and computer graphics. He has served as a Program Committee Member of SIGGRAPH and SIGGRAPH Asia.

Enhua Wu (M'12) received the B.Sc. degree from Tsinghua University, Beijing, China, in 1970, and the Ph.D. degree from The University of Manchester, Manchester, U.K., in 1984. He is currently a Research Professor with the State Key Laboratory of Computer Science, Institute of Software, Chinese Academy of Sciences, Beijing, China. He is also an Emeritus Professor with the University of Macau, Macau, China. His current research interests include realistic image synthesis and virtual reality. He is a Member of the ACM and a Fellow of the China Computer Federation. He has served as a Chair or Co-Chair for various conferences, including SIGGRAPH Asia 2016. He is an Associate Editor-in-Chief of the *Journal of Computer Science and Technology*.